

Research Paper

Insights into drop-on-demand metal additive manufacturing through an integrated experimental and computational study

N. Gilani^{*}, N.T. Aboulkhair, M. Simonelli, M. East, I. Ashcroft, R.J.M. Hague

Centre for Additive Manufacturing, Faculty of Engineering, University of Nottingham, Nottingham NG8 1BB, UK

ARTICLE INFO

Keywords:

Drop-on-demand
Metal jetting
Thermo-mechanical simulation
Additive manufacturing
Interface
Metal droplets

ABSTRACT

Drop-on-demand metal jetting is a recent additive manufacturing technology opening new opportunities for the fabrication of complex single and multi-metal components. MetalJet, the Océ developed technique used in this study, has the capacity to produce molten micro-droplets (60–80 μm) at temperatures up to 2000 $^{\circ}\text{C}$ to form single and multi-material objects. Applications for this technology include flexible circuits, advanced electronic components and biotechnologies. However, full exploitation of this technology is impeded by a lack of understanding of various aspects of the process, including droplet bonding and interface formation, residual stress development and the evolution of microstructure. This paper uses an integrated numerical and experimental approach to provide insights into these research questions. Thermal models were used to investigate droplet-to-substrate adhesion and explain the experimentally-observed morphology of droplets. Thermo-mechanical modelling was used to investigate residual stress development and its role in the observed droplet warping and delamination. The knowledge obtained from this study can be used to underpin the development of functional multi-material printing.

1. Introduction

Metal jetting, also known as liquid metal jet printing, is a nascent additive manufacturing (AM) technology that has the potential to fabricate metallic components, both single and multi-material, at a resolution not achievable with the more common powder fusion based additive manufacturing techniques. The process primarily consists of dispensing and depositing individually-controlled droplets of molten metal onto a substrate at precise locations. From an operational perspective, there are similarities between metal jetting and micro-casting, spray shape deposition manufacturing (SDM) [1], and thermal spraying [2]. However, the control over the size of droplets, jetting speed and the precision of manufacturing set metal jetting apart from these other processes. Moreover, metal jetting has advantages over other AM technologies, such as Laser Powder Bed Fusion (L-PBF), Directed Energy Deposition (DED), and binder jetting due to its simplified fabrication approach. This simplicity is granted by the elimination of the need for pre-processing, such as powder handling, and post-print processing, such as, polishing or grinding to achieve an acceptable surface finish. In addition, the extended degree of freedom in metal jetting promises new avenues in fabricating functional multi-material metallic

devices. However, critical elements of the process, such as droplet-substrate adhesion, droplet-droplet coalescence, cooling and solidification, and residual stress evolution, which all define the consistency and quality of printed parts, are still not well understood. This limits optimisation of the process for particular applications and poses a challenge to the ultimate exploitation of the technology.

In metal jetting, molten material is ejected in either a continuous or drop-on-demand (DOD) fashion. In the DOD method, well-defined droplets are expelled from a nozzle in a periodic or aperiodic controlled manner, resulting in a highly precise printed component, making it advantageous compared to continuous jetting [3]. The various mechanisms of actuation in DOD printing include pneumatic [4–6], piezoelectric [7,8], and Magneto-Hydro-Dynamic (MHD) actuators. The first two are either limited in the droplet size ($> 200 \mu\text{m}$), frequency of droplet generation ($< 200 \text{ Hz}$), or to low melting point materials ($< 700 \text{ }^{\circ}\text{C}$). The MHD technique has been the subject of a number of studies [9–11] and has been shown to overcome the limitation of droplet generation frequency seen in other DOD methods. MetalJet [12], a novel DOD metal jetting additive manufacturing technology based on the MHD principle, was the first to overcome the melting point and droplet size limitations, listed above, concurrently. The MetalJet printheads, originally patented by Océ (now Canon Production Printing) [13],

^{*} Corresponding author.

E-mail address: negar.gilani@nottingham.ac.uk (N. Gilani).

| Nomenclature | |
|-----------------|--|
| K_{eff} | Effective thermal conductivity ($W/m^{\circ}C$) |
| c_{mf} | Conductivity multiplier factor |
| K | Thermal conductivity ($W/m^{\circ}C$) |
| L | Latent heat of solidification (KJ/Kg) |
| Nu | Nusselt number |
| x | Droplet's height (m) |
| r | Droplet's radius (m) |
| R_c | Thermal contact resistance ($m^2^{\circ}C/W$) |
| k_c | Thermal conductance coefficient ($W/m^2^{\circ}C$) |
| R_a | Surface roughness |
| α_t | A user-defined parameter to correlate thermal resistance to surface tension and contact pressure |
| ρ | Density (Kg/m^3) |
| C_p | Heat capacity ($J/Kg^{\circ}C$) |
| σ_s | Surface tension (N/m) |
| ϵ_{em} | Emissivity |
| h | A user-defined combined radiative and convective heat transfer coefficient ($W/m^2^{\circ}C$) |
| h_{conv} | Free heat convection coefficient ($W/m^2^{\circ}C$) |
| σ_{SB} | Stefan-Boltzmann constant ($W/m^2^{\circ}C^4$) |
| T_{surf} | Surface temperature ($^{\circ}C$) |
| T_{∞} | Ambient temperature ($^{\circ}C$) |
| T | Temperature ($^{\circ}C$) |
| T_s | Substrate temperature at the interface ($^{\circ}C$) |
| T_d | Droplet temperature at the interface ($^{\circ}C$) |
| σ | Stress (MPa) |
| ϵ | Strain |

produce micro metallic droplets ($< 80 \mu m$ in diameter) of high temperature (up to $2000^{\circ}C$), at frequencies up to 2 kHz. The capabilities of the system in the digital printing of 3D structures with high degrees of accuracy and precision have been demonstrated by Simonelli et al. [12]. Owing to its novelty, the physical factors, governing the quality and properties of the net-shapes produced by the system are yet to be comprehensively understood. This consists of temperature at the interfaces, which defines the level of bonding, the cooling rate, which is one the key factors to control for a desired microstructural development, and the residual stresses, which may lead to distortion and/or de-bonding. However, investigating these important aspects of the process experimentally is challenging due to the resolution limitations of the experimental techniques available and the time and size scales involved. A powerful alternative method of investigation is via computational simulation of the process, though this also faces challenges and limitations.

There have been several attempts to simulate the spreading and solidification of single and multiple droplets depositions. While 2D models are not capable of capturing all the details of the deposition process [14, 15], 3D models [16–18] require a large computational effort due to the complex nature of the problem. This may necessitate the implementation of a coupled multi-physics model involving fluid flow, heat transfer and solid mechanics. In order to manage this complexity in a computationally efficient modelling approach, droplet spreading has been considered a precursor to droplet solidification in some studies, thus the droplet geometry was kept constant during the heat transfer solution [19–22]. Although these models have the advantage of computational efficiency, they also introduce some limitations in accurately representing the temperature distribution within the droplet and substrate during cooling. Firstly, they neglect the thermal resistivity between the droplet and substrate, thereby overestimating the droplet cooling rate and substrate peak temperature. Secondly, some models do not consider the convective flow effect in the liquid metal. Despite the diversity of research to simulate the thermal profile of droplets during deposition, there have been relatively few attempts to simulate the evolution of residual stresses on cooling and solidification. In [23–25], 1D thermo-mechanical models were used, where mechanical solutions have

accuracy limitations due to the inability of 1D thermal solutions to accurately represent the multi-dimensional conduction effects seen in practice.

The main objective of this research is to better understand the MHD metal jetting (MetalJet) process, further explain the experimental observations, and investigate issues such as lack of adhesion at interfaces, residual stress, and related delamination. This is achieved through an integrated experimental and computational approach. For this purpose, single and multiple droplets were deposited onto substrates using our experimental, non-commercial MetalJet process and were characterised. In parallel, a computational model was established to predict the thermal evolution of the droplets and substrate, as well as the residual stress evolution during the deposition of single and multiple droplets. The intensive computational effort to simulate the spreading dynamics of droplets was avoided by utilising the experimentally observed droplet morphology and implementing this into a 3D Finite Element (FE) thermo-mechanical model. However, the convective effects in the liquid droplet were still taken into account through application of a modified thermal conductivity for the liquid metal. The thermal resistance between the droplet and substrate, and temperature-dependent material properties were also considered. It is considered that this combined experimental and 3D thermo-mechanical modelling approach provides a sufficiently accurate and computationally efficient method of investigating the MetalJet process to achieve the aims of the study.

2. Methods

Fig. 1 illustrates the overall approach adopted in this article, which consists of an integrated computational and experimental method. In the characterisation of MetalJet samples, in both this work and the literature [12], various features have been observed which require further investigation. However, the narrow temporal and spatial scales contained within the process do not allow in-situ measurement at the required resolution, thus the need to apply numerical simulations to obtain complementary insights. The experimental and numerical approaches are explained individually in the following sections.

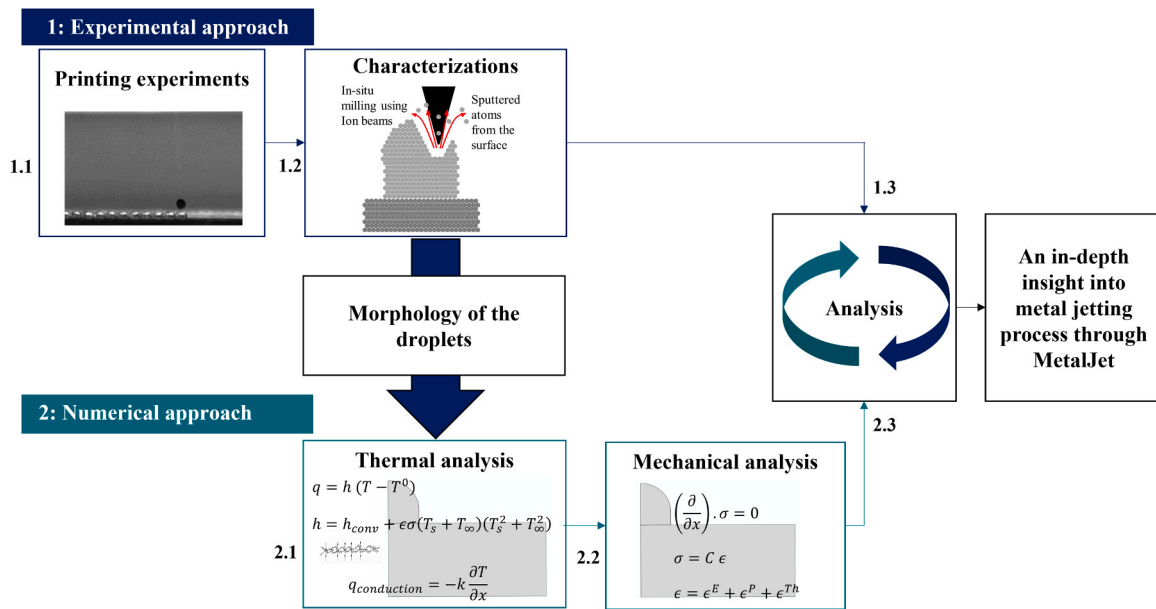


Fig. 1. Schematic presentation of the hybrid approach used in this research.

2.1. Experimental methods

2.1.1. Materials

The main focus of this article is to study the thermomechanical behaviour of high-temperature metallic (> 1000 °C) microdroplets during solidification and cooling. Therefore, pure Cu was chosen for droplet and substrate material due to it being within the operational parameters of the equipment and also highly useful for many applications requiring high conductivity. Pure Cu rods, of grade 5N, supplied by ESPI Metals (Oregon, USA) were used as feedstock for jetting. 1 mm thick tempered Cu sheets of 99.9% purity supplied by Advent research materials (Oxford, UK) were used as substrates. These substrates were polished using SiC papers grit sizes 2500 to remove surface oxides immediately prior to experiments. In order to provide some validation of the numerical model used in this work, in particular the proposed relation for the thermal resistance coefficient and effective thermal conductivity multiplier, pure Sn (grade 5N) droplets with various droplet/substrate temperatures were deposited on Sn substrates. Sn was chosen for these validation studies since its low melting point provides the condition of substrate melting, which could be used to validate the proposed model.

2.1.2. Droplet deposition and experimental set-up

In order to investigate the adhesion of droplets to the substrate, inter-droplet bonding, and provide some validation of the numerical model used in this study, individual and multiple droplets were deposited onto a substrate. These metal deposition experiments were conducted using an experimental and bespoke DOD AM technology, MetalJet, in which Cu microdroplets of ~ 78 μm in diameter are generated using a Magneto-Hydro-Dynamic (MHD) actuation system [13]. Initially, the material is melted inside a graphite cartridge by induction heating and flows toward the orifice by gravitation. Close to the orifice, a magnetic field is produced by two permanent magnets with a magnetic flux density (B) of 2 T. A variable electrical current (I), in the range of 20 A to 120 A, is provided through two tungsten electrodes, which are in contact with the liquid metal via the cartridge, and are placed perpendicular to the magnetic field direction. As a result, a manageable Lorentz force ($\vec{F} = \vec{I} \times \vec{B}$) is provided to eject droplets through the orifice. By setting the centre-to-centre distance between droplets and frequency of jetting, the substrate speed is automatically calculated such that droplets are

successively deposited onto the desired locations according to the geometry described by a CAD (Computer-Aided Design) file. The substrate is placed on a stage controller, which can be heated up to 500 °C. In order to prevent oxidation during jetting, the system is kept inside an argon-controlled atmosphere glove-box, maintaining the oxygen content under 1 ppm. The jetting frequency is adjustable from 10 to 2000 Hz but was kept constant at 500 Hz in this work, with a jetting speed fixed at 2 m/s for Sn droplets and 1 m/s for Cu droplets. In order to minimise the in-flight time, and consequent heat loss, the working distance, i.e. the distance between the nozzle and substrate, was set to 1 mm. Cu droplets were ejected at 1120 °C, and substrate temperature was fixed at 500 °C. Successive Cu droplets were deposited at 500 Hz (time interval of 2 ms) and a centre-to-centre distance of 72 μm , i.e. an overlap of 6 μm . For the model validation, Sn droplets were ejected at 670 °C, 775 °C, and 985 °C onto Sn substrates at 50 °C and 100 °C. The in-flight cooling before impacting the substrate was calculated [12]. Consequently, Cu and Sn droplets were deposited onto the corresponding substrates at 1090 °C, 655 °C, 755 °C, and 955 °C, respectively.

2.1.3. Characterisation

The morphology of single and multiple overlapping Cu droplets, their microstructure, the bonding at droplet-to-droplet, and droplet-to-substrate interfaces were examined using an FEI Quanta 200 3D Dual Beam FIB-SEM (FEI, Hillsboro, Oregon, USA). The focussed ion beam (FIB) was used initially for cross-sectioning portions of droplets by in-situ stress-free milling. The cross-sections were etched using these ion beams, and finally, crystallographic orientation contrasts were captured in FIB secondary electron images. A Jeol 7100 FEG-SEM equipped with Oxford Instruments AZtec HKL Advanced Electron BackScatter Diffraction (EBSD) system (Oxford Instruments plc, Abingdon, UK) was used for further microstructural observation of the prepared cross-sectioned samples. The surface roughness of substrates was measured using an optical 3D measurement system, Alicona InfiniteFocusG4 (Alicona Imaging GmbH, Graz, Austria).

2.2. Finite-element model

A sequentially coupled thermo-mechanical model was established using a commercial FE package, ABAQUS/ standard, version 2019 (Dassault Systèmes Simulia Corp.), to simulate droplet deposition in the MetalJet process. It was assumed that the stress and deformation were

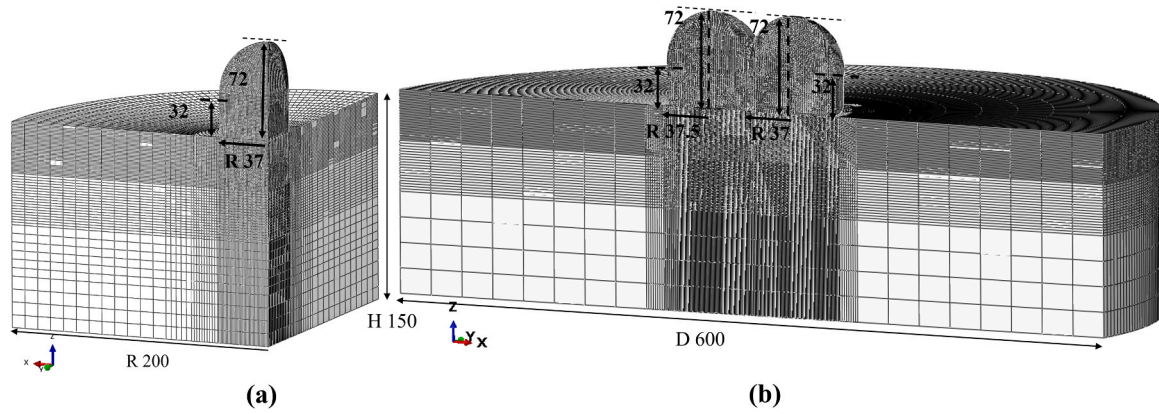


Fig. 2. Geometries and mesh distribution of droplet and substrate for a) single droplet deposition, and b) multiple droplet deposition model.

dependent on the temperature field, whereas the temperature is not a function of the deformation response, i.e. one way coupling. This is regarded as a realistic consideration since the displacements are small and hence, have little effect on heat generation or distribution. The thermal model predicts the temperature evolution of the droplets and substrate during the deposition process. In this study, the phenomena of interest, mainly occur in the solid phase and the shape of the solid droplets were taken from experimental observations. Hence, the fluid dynamics of impact and spreading were not modelled. However, the effects of convective heat transfer due to the droplet motion were integrated into the modelling approach used by the implementation of an effective thermal conductivity for the liquid metal. The droplet was considered a continuum body, and its shape was reproduced from the experimental observations. The liquid thermophysical properties were applied to the droplets' sections above the Cu melting point. The mechanical model provides information on the consequent residual stresses and deformations due to the thermal changes during the cooling process.

2.2.1. Thermomechanical model definitions

The transient temperature distribution throughout the domain was obtained by solving the three-dimensional heat conduction (Eq. (1)), in the droplet and substrate along with the appropriate initial and boundary conditions.

$$\frac{\partial}{\partial x} \left(K_x \frac{\partial T}{\partial x} \right) + \frac{\partial}{\partial y} \left(K_y \frac{\partial T}{\partial y} \right) + \frac{\partial}{\partial z} \left(K_z \frac{\partial T}{\partial z} \right) + Q = \rho C_p \frac{\partial T}{\partial t} \quad (1)$$

Where K is the temperature-dependent thermal conductivity, T is the temperature, Q is the power generated per unit volume, ρ is the material density, and C_p is the heat capacity.

The thermal boundary conditions constitute combined convection and radiation from the free surfaces and conduction between the droplet and substrate. The convection and radiation heat exchange at the free surfaces of droplet and substrate were implemented according to Newton's law of cooling:

$$q_{conv-rad} = h(T - T_\infty) \quad (2)$$

where T_∞ is the ambient temperature equal to 30 °C, and h is a user-defined heat transfer coefficient. To consider the effects of heat radiation but avoid the consequent computational non-linearities, a radiative and convective heat transfer coefficient was used based on the equation proposed by Mughal et al. [26]:

$$h = h_{conv} + \epsilon_{em} \sigma_{SB} (T_{surf} + T_\infty) (T_{surf}^2 + T_\infty^2) \quad (3)$$

where ϵ_{em} is the emissivity and equal to 0.1, σ_{SB} is the Stefan-Boltzmann constant ($5.67 \times 10^{-8} \text{ W/m}^2\text{C}^4$), and h_{conv} is the free heat convection ($\cong 40 \text{ W/m}^2\text{C}$).

The conductive heat transfer between the droplet and substrate interfaces is defined by:

$$q_{cond} = k_c(T_s - T_d) \quad (4)$$

where k_c is the thermal conductance coefficient, T_d is the droplet temperature at the interface with the substrate, and T_s is the substrate temperature at the interface with the droplet.

Uniform initial temperatures of 1090 °C and 500 °C were assigned to the droplet and substrate, respectively. The temperature at the bottom surface of the substrate was kept constant and equal to 500 °C throughout the simulation. Adiabatic conditions were applied to the droplet and substrate's symmetric surfaces (XZ and YZ planes for the single droplet and XZ plane for multiple droplets).

The stress equilibrium in the mechanical model is governed by:

$$\nabla \cdot \sigma = 0 \quad (5)$$

The mechanical constitutive law is defined by:

$$\sigma = C \epsilon^E \quad (6)$$

Where C is the fourth-order material stiffness tensor and ϵ^E is the elastic strain.

The total strain can be decomposed into three components:

$$\epsilon = \epsilon^E + \epsilon^P + \epsilon^{Th} \quad (7)$$

Where ϵ^{Th} is the thermal strain arising from the differential thermal contractions and expansions and is computed using the temperature-dependent coefficient of thermal expansion. The plastic strain (ϵ^P) is calculated from the flow rule given by Prandtl-Reuss equations, with the Von Mises yield criterion. Close to the recrystallisation temperatures, residual stresses may cause creep strain, however as the temperature decreases, there is a steep drop in the creep rate, and for temperatures less than half the solidus temperature, creep becomes negligible. Since the cooling rate in the MetalJet process is extremely high, in the range of 10 to 10^4 °C/ms, the time at elevated temperature is short enough to ensure creep is negligible.

A stress-free initial condition was considered, and symmetrical conditions ($U_x = UR_y = UR_z = 0$ at YZ plane and $U_y = UR_x = UR_z = 0$ at XZ plane for the single droplet) were applied to the symmetry planes of the droplet and substrate. The bottom surface of the substrate was constrained in all displacement and rotations. A tie constraint, i.e. perfect bonding, between the droplet and substrate was assumed, which ensures no relative motion between the contact surfaces.

The use of quarter-symmetry and half-symmetry models to simulate single and multiple droplet deposition, respectively, is shown in Fig. 2. The substrate dimensions were chosen to avoid excessive computational cost whilst being able to capture the depth to which the heat diffused in the analysis time.

Table 1
Temperature-dependent properties of pure Cu.

| Temperature (°C) | 27 | 227 | 427 | 627 | 827 | 1027 | 1200 |
|---|------|------|------|------|------|------|------|
| Density Kg/m ³ | 8960 | 8762 | 8564 | 8366 | 8168 | 7971 | 7800 |
| Surface tension (N/m) | – | – | – | – | – | – | 1.28 |
| Heat capacity (J/Kg °C) | 385 | 408 | 425 | 441 | 464 | 506 | 520 |
| Thermal conductivity (W/m °C) | 401 | 386 | 372 | 359 | 345 | 331 | 319 |
| Thermal expansion (1/°C) × 10 ⁻⁶ | 15.4 | 16.9 | 18.5 | 20.1 | 21.9 | 23.7 | 25 |
| Young modulus (GPa) | 125 | 112 | 98 | 85 | 72 | 58 | 4 |
| Yield strength (MPa) | 210 | 181 | 66 | 20 | 10 | 2 | 0.1 |
| Ultimate tensile strength (MPa) | 250 | 200 | 105 | 30 | 18 | – | – |

2.2.2. Parameters and material properties

The thermo-physical properties of the material, including density, heat capacity and thermal conductivity, were considered temperature-dependent and isotropic. A finite temperature range of 4 °C was considered for the solidification of pure copper (1087–1083 °C), during which latent heat of 205 KJ/Kg is released. The temperature gradient inside the molten droplet results in surface tension variation that drives Marangoni-type flow. Since the fluid motion of the droplet was not analysed, its consequent forced convective heat transfer was accounted for by the use of an effective thermal conductivity. Therefore, when the temperature of the metal was above its melting point, K_{eff} , using the equation suggested by Zarzalejo et al. [21] was activated:

$$K_{eff} = c_{mf} K \quad (8)$$

where K_{eff} is the effective thermal conductivity and c_{mf} is the conductivity multiplier factor, which is greater than one and is a function of the Nusselt number (Nu), the droplet height (x), and the interface length. c_{mf} has been experimentally measured in various studies [1,21,27] and is equal to 2.

The thermal contact property at the interface of two surfaces depends on various parameters, such as flatness, surface roughness, and hardness. This is defined by the thermal contact resistance, R_c , or the thermal conductance coefficient, which have a reciprocal relation:

$$k_c = 1/R_c \quad (9)$$

Although it is well known that this parameter has a major influence on the heat transfer between two surfaces, in previous work from others it has either been arbitrarily chosen [14,17] or neglected altogether [1, 11,21,24] due to the lack of information on how to estimate it. In some prior research, this parameter was experimentally measured, however, the response time of temperature sensors is usually longer than the spreading time of the droplets, which can lead to inaccuracies in the results. Aziz et al. [28] calculated the thermal contact resistance

between molten Sn droplets and a stainless-steel substrate by matching the measured surface temperature variation with an analytical solution. Their measured values varied between $10^{-6} m^2K/W$ and $5 \times 10^{-6} m^2K/W$. Similarly, Kumar et al. [15] estimated the thermal contact resistance between Al–33 wt% Cu droplets and stainless steel at $7 \times 10^{-4} m^2K/W$. Trapaga et al. [14] considered several values of thermal resistance ranging between $10^{-4} m^2K/W$ and $10^{-6} m^2K/W$ for Cu droplet impinging on a Cu substrate. In this study, we have modified the relation established by Xue et al. [29] to estimate a temperature-dependent thermal resistance:

$$R_c = R_a / (K\alpha_t) \quad (10)$$

in which R_a is the surface roughness and equal to 0.01 μm . α_t is a unitless parameter, which depends on surface tension and contact pressure and is defined in this work as:

$$\alpha_t = 2\pi r \rho g x / \sigma_s \quad (11)$$

in which r is the droplet radius, and σ_s is the surface tension. For the solidified material, α_t is considered constant and equal to its value at the liquidus temperature. It should be noted that this relation is applicable only if the substrate asperities scale (R_a) is considerably smaller than the droplet height.

The mechanical properties: Young's modulus, coefficient of thermal expansion, and yield stress, were also considered temperature-dependent and isotropic. Since a non-zero value for the yield strength is required by the numerical solver, a relatively small value of 0.1 MPa was used at temperatures above the solidus temperature. The Poisson's ratio was assumed to be 0.35 and temperature independent. The thermo-mechanical properties ranging from room temperature to 1200 °C are listed in Table 1 [30].

2.2.3. Mesh and time step

The thermal and mechanical models utilised identical nodal

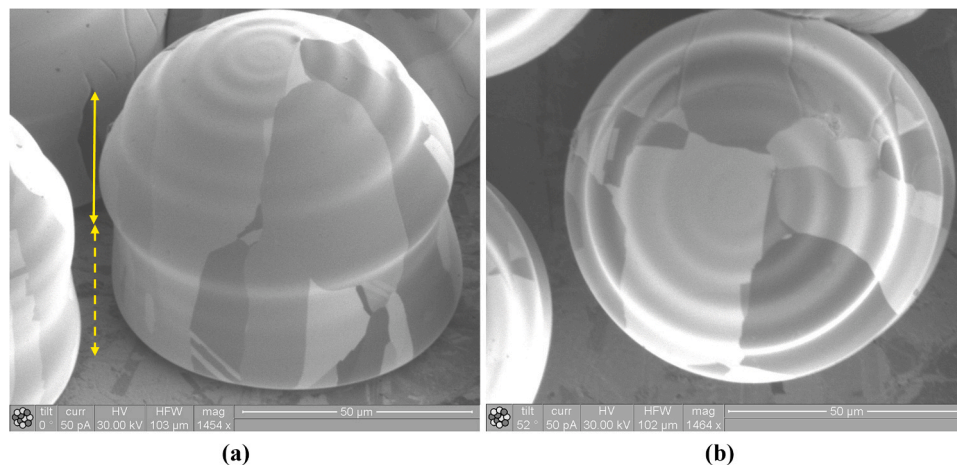


Fig. 3. Morphology of single Cu droplet deposited on a Cu substrate, forming ripples on their periphery during the solidification: **a)** side view, **b)** top view. (For interpretation of the references to colour in this figure legend, the reader is referred to the web version of this article.)

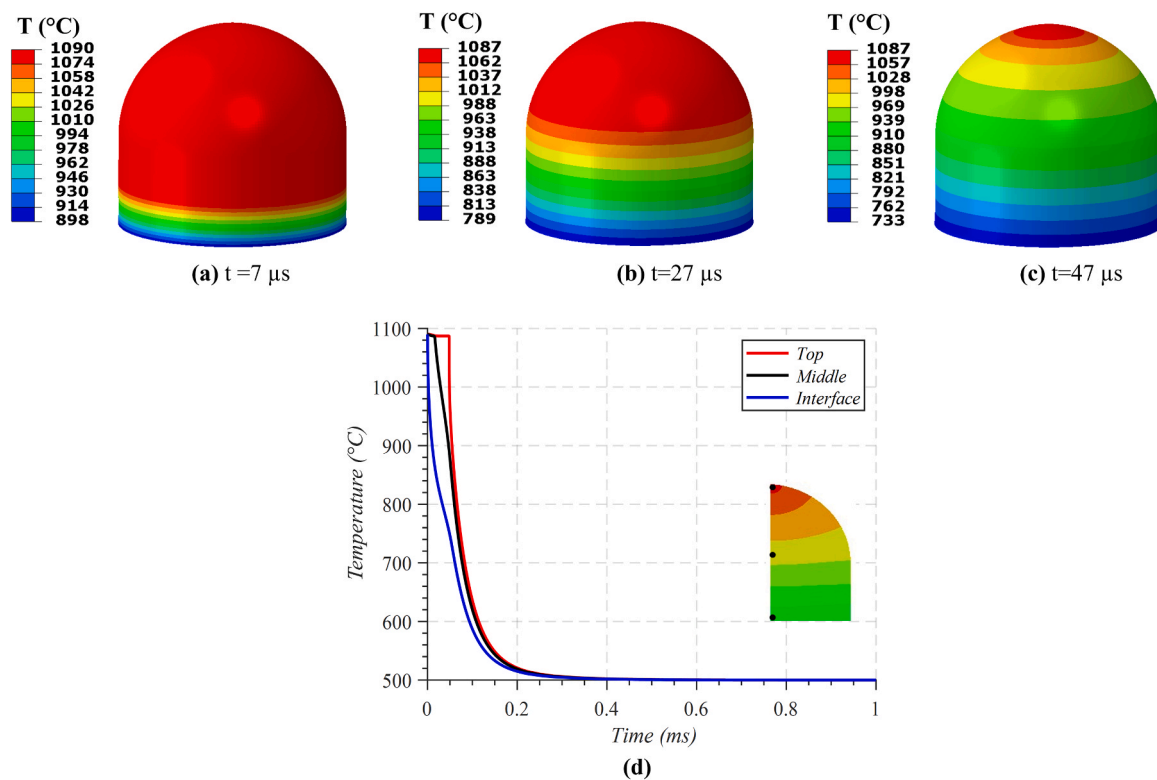


Fig. 4. 3D profile temperature whilst single Cu droplet cooling onto a Cu substrate, taken at a real-time of a) $t = 7 \mu\text{s}$, b) $t = 27 \mu\text{s}$, c) $t = 47 \mu\text{s}$, d) temperature evolution of nodes in the top, middle, and interface of the droplet.

locations to simplify coupling, the meshes for the single and multiple droplets are shown in Fig. 2. A mesh convergence study was initially performed. Accordingly, a uniform hexahedral mesh with element length of $1 \mu\text{m}$ was used for the droplet, resulting in 46,512 elements for a single droplet and 300,235 for the multiple droplet model. A non-uniform density mesh was used for the substrate, with an element length of $1 \mu\text{m}$ close to the interface, where the temperature and displacement gradients are steepest, gradually increasing towards the bottom and sides. This meshing strategy resulted in a total of 96,668 elements for the substrate in the single droplet model and 433,161 in the multiple droplet model. In the mechanical model, reduced integration elements were used to enhance the convergence behaviour.

A transient heat transfer and a general static analysis with an initial time step of 10^{-9} s was used to solve the thermal and mechanical problems, respectively. Automatic time steps were activated in the thermal and mechanical models so that the sizes of subsequent time increments were automatically adjusted based on the required time for the solution to converge. The initial time step was chosen to effectively capture the effects of the fast cooling rate in the process. A typical thermo-mechanical simulation of a single droplet required 53 h of CPU time, whereas the thermal simulations of multiple droplets took approximately 71 h of CPU time using 8 processors of Intel Xeon Silver 4210@3.20 GHz, and the GPU acceleration was enabled using an NVIDIA Quadro RTX 5000.

3. Experimental and computational results

In this section, various features of deposited droplets and their characterisation are analysed using a combined experimental-computational approach. The thermal model validation is presented in Appendix A.

3.1. Morphology of droplets

Cu droplets of $\sim 78 \mu\text{m}$ in diameter at $1090 \text{ }^\circ\text{C}$ were deposited on a

Cu substrate kept at $500 \text{ }^\circ\text{C}$. As the droplets contact the substrate, they spread and solidify, forming ripples on the droplet's periphery, as can be seen in the FIB-SEM images in Fig. 3. Ripples have also been reported in previous works [17,31]. However, in this study, the striations are more widespread. The formation of ripples, in particular the distance between their peaks, is a function of solidification and oscillation rates [32]. It is likely that the droplets solidify practically instantly at the moment of impact in the bottom portion (yellow dashed double arrow) such that the solidification rate is greater than the oscillation rate, leaving no ridges. Whilst in the top portion (yellow double arrow), where solidification is slower, the droplet oscillates, spreading and recoiling. If solidification occurs during this oscillation, the observed ripples are frozen into the droplet surface. The results from the computational thermal analysis of a single droplet cooling on a substrate are used to support this argument.

According to the thermal profile of a single Cu droplet at $1090 \text{ }^\circ\text{C}$ deposited onto a $500 \text{ }^\circ\text{C}$ Cu substrate in Fig. 4 a-c, solidification initiates at the interface, where the droplet is in direct contact with the cooler substrate. Indeed, conduction with the substrate, which acts as a heat sink, is the dominant mode of cooling. The solidification front moves upwards through the droplet and in less than $50 \mu\text{s}$ after impact, the entire droplet solidifies. After 1 ms, the droplet reaches steady-state, i.e. the droplet temperature is uniform and equal to the substrate temperature. This is faster than the time interval before the deposition of the second droplet using a jetting frequency of 500 Hz, which is equal to 2 ms. Comparing the experimental results versus computational results, the ridges observed in Fig. 3 follow the solidification planes predicted by the numerical simulation (Fig. 4). As per the droplet temperature evolution in Fig. 4 d, the material freezes practically instantly at the interface when it contacts the cooler substrate, whilst remaining liquid in the top section. Solidification in the uppermost sections is slower for two reasons: (1) cooling through convection and radiation is negligible compared with cooling through conduction with the substrate, and (2) the release of latent heat during solidification. Towards the bottom of the droplet, the latent heat energy is invested in heating the substrate

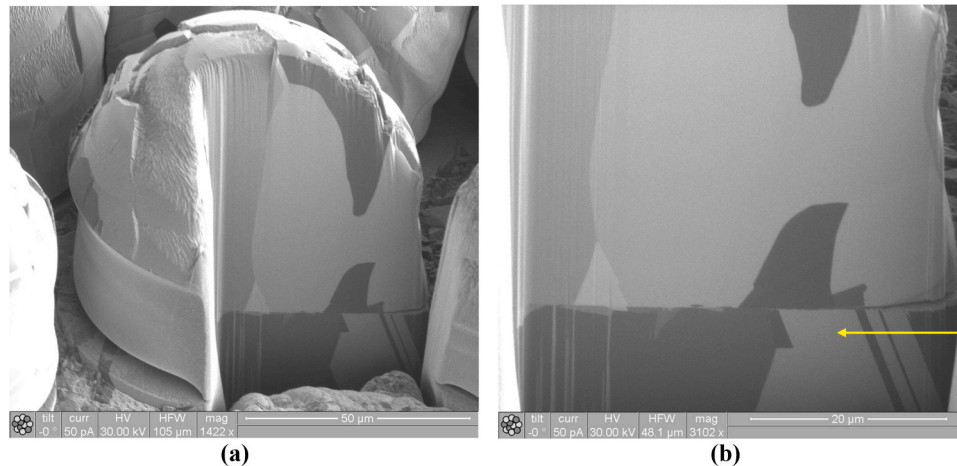


Fig. 5. FIB-SEM cross-section of individual Cu droplet deposited on a Cu substrate showing: **a)** droplet's polycrystalline microstructure with large grains, **b)** absence of substrate remelting or diffusion at the interface, and droplet delamination in the edges.

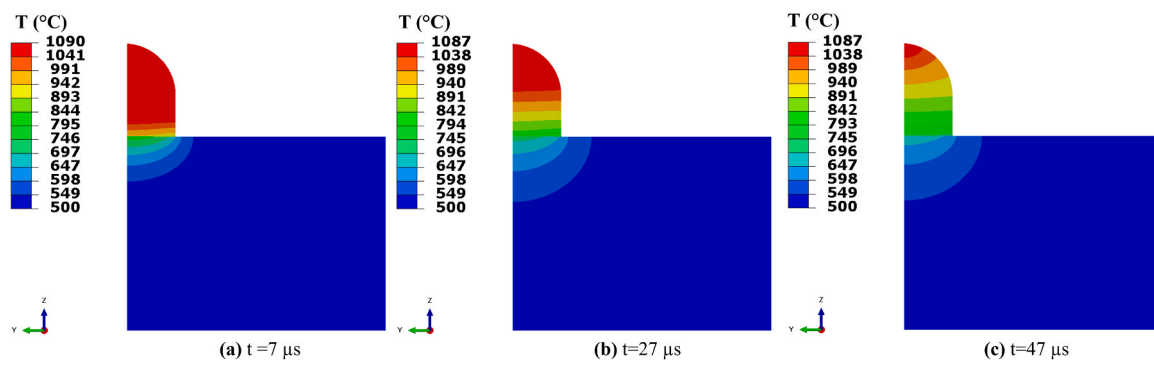


Fig. 6. Cross-sectional profile views of temperature during single Cu droplet deposition onto a Cu substrate, taken at a real-time of **a)** $t = 7 \mu\text{s}$, **b)** $t = 27 \mu\text{s}$, **c)** $t = 47 \mu\text{s}$ after deposition.

and has a minor influence on the droplet's cooling speed. Contrarily, in the top section of the droplet, cooling is slowed by release of the latent heat of solidification. Indeed, the computational modelling proves that the presence of more ridges at the top sections of the droplet is due to the differential solidification rates.

We propose that the various observations in the literature regarding droplet ripples can be attributed to the use of different droplet and substrate materials, different droplet sizes, and different droplet initial temperatures. All of these factors will affect the rate of solidification and/or frequency of oscillation of a droplet, which in turn affects whether, and where the oscillatory movement of the droplet will be 'frozen in'. For example, in [17] and [30], the wavelength of striations on the surface of droplets decreased bottom up, such that there were no ridges on the top section of droplets. Three factors contribute to the contradictory observation regarding the pattern of these ridges in the mentioned literature and this study. Firstly, these findings were reported for Al and Al alloy droplets printed onto a Ni substrate. The Cu substrate and Cu droplets used in our study, have a higher thermal conductivity than the Ni substrate and Al droplets, inducing a faster solidification, in particular close to the interface. Secondly, the size of droplets in those studies was 1.5 mm in diameter. The smaller droplets in our study dissipate their thermal energy to the substrate at a higher rate. Thirdly, in our research, droplets were deposited just above their melting point, whereas in previous studies, the liquid metal was superheated to 100 °C or 200 °C above the melting point. These three facts result in a slower cooling rate in those studies, which in turn lead to simultaneous progress of solidification front into the oscillating liquid, hence the formation of ripples in the bottom sections. In the top section, with the slower rise of the solidification front, the viscosity damped oscillations and left no striation trace behind. In our study, the solidification time was faster

than one oscillation interval in the bottom section where no ripple is formed. Only in the top section, where solidification is relatively slower, striations are formed based on the explained mechanism.

3.2. Droplet to substrate bonding

In the cross-sectional view of a single droplet shown in Fig. 5, the interface line between the droplet and substrate is clearly visible. It was also observed that the droplet was only loosely attached to the substrate, confirming the absence of substrate melting to form a fusion (metalurgical) bond between the droplet and substrate. A similar issue was reported in [12] for Ag droplets deposited onto a Cu substrate. Moreover, there was no sign of a preferential grain orientation due to a potential epitaxial growth at the interface, consequently, no interdiffusion has occurred. Also, a gap can be seen between the droplet and substrate at the droplet's edge, which is indicative of distortion of the droplet due to residual stresses (this is marked in Fig. 5 b by a double-headed arrow). What is not clear without further investigation is whether the residual stress caused delamination at the interface or whether it is the lack of bonding at the interface resulting in no constraint from the substrate to residual stress-induced deformation. Another feature observed in Figs. 3 and 5 is that the droplet has a polycrystalline microstructure with large grains, suggesting heterogeneous nucleation over the substrate surface. The heterogeneous nucleation is attributed to the imperfections on the substrate caused by polishing, yielding the initial nucleation sites. Also, the surface defects provide the condition for adequate undercooling (supercooling) in the absence of impurity in the deposited droplet. However, the low crystallites suggest a low nucleation rate, which is a result of a small undercooling. The latter can be attributed to the poor contact at the interface. It is also observed that the grains are directed

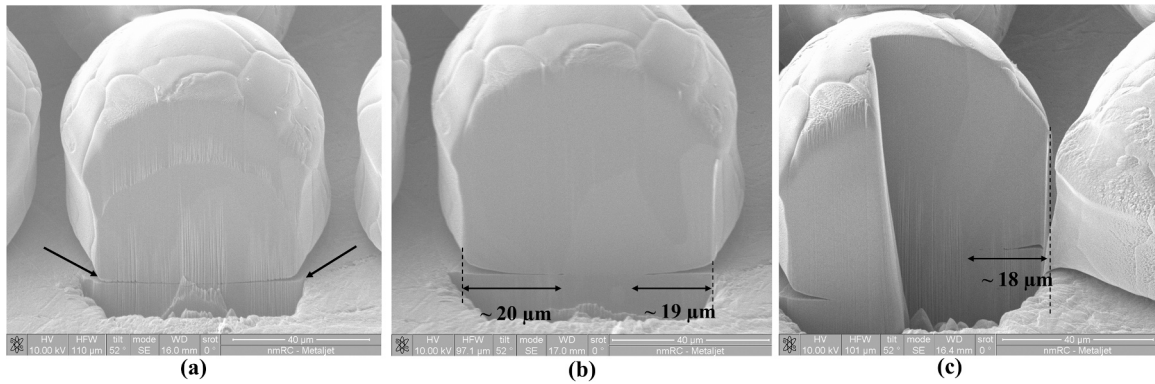


Fig. 7. SEM cross-section of individual Cu droplet after FIB milling of: a) 16 μm , b) 20 μm , c) 45 μm from the edge showing the partial delamination of the droplet from the Cu substrate.

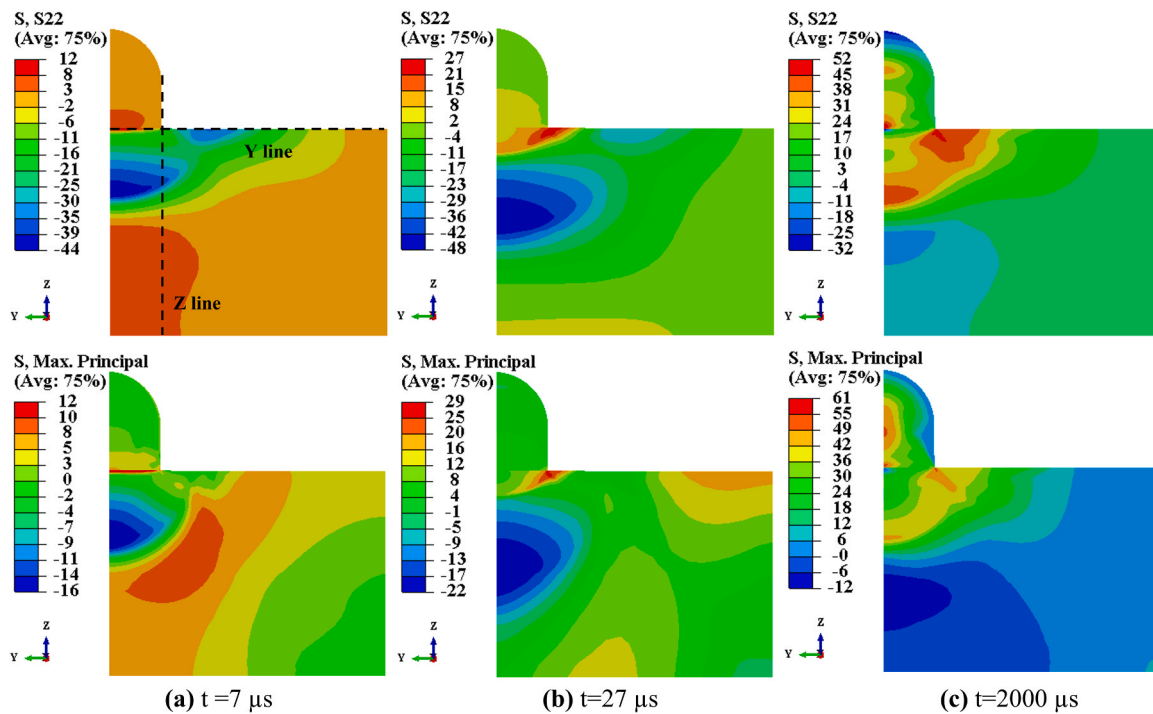


Fig. 8. σ_{yy} and $\sigma_{Max\ principal}$ stress fields (MPa) in the Y-Z plane whilst first Cu droplet cooling onto a Cu substrate at real-time of a) $t = 7 \mu\text{s}$, b) $t = 27 \mu\text{s}$, and c) $t = 2000 \mu\text{s}$ after deposition.

from the substrate interface toward the droplet’s top, indicating a directional heat flux.

The cross-sectional views of the droplet and substrate thermal profile obtained by numerical simulations in Fig. 6 a–c show the substrate heating from contact with the droplet. It can be seen that the affected area of the substrate is quite local to the contact site, which is not surprising given the small mass of the droplet and hence the amount of thermal energy available for transfer to the substrate. The substrate temperature reaches a maximum value of 760 °C at the central point of the interface, which is far below the melting point of Cu (1084 °C). This temperature is also below the required temperature to promote the diffusion of Cu atoms between the two surfaces [33], particularly as this level of high temperature is maintained only for a few tens of microseconds. Consequently, metallic bonds are not formed at the interface,

and droplets are attached to the substrate through physical adsorption (physisorption), in which droplet’s molecules are attracted toward the substrate molecules by weak Van der Waals forces. This explains the poor droplet-to-substrate bonding observed in the experimental results.

3.3. Stress analysis of a single droplet

The non-uniform temperature distribution in the droplet on cooling and between droplet and substrate results in differential thermal contractions and, hence, transient residual stress. A high gradient of residual stresses at the substrate-droplet interface can cause separation of the droplet from the substrate, i.e., delamination. The cross-sectional SEM images of a single droplet, where 16 μm and 20 μm from the edge were removed, are shown in Fig. 7 a-b, respectively. The droplet seems to be

detached from the substrate in Fig. 7 a, while in Fig. 7 b, it is partially bonded to the substrate in the central region and de-bonded at the edges. In Fig. 7 c, further material was removed, to a depth of 45 μm from the edge. It is seen that the de-bonded region at the edge was persistent. In general, it seems the droplet is lifted from the substrate at the free edges and the separation subsequently propagates toward the centre of the droplet. The source of such phenomenon is probably the residual stresses; hence, it is essential to understand how they develop in order to mitigate their consequences.

Fig. 8 a–c illustrate the transversal (σ_{yy}) and maximum principal stress fields in the droplet and substrate on the Y-Z plane at various time frames (refer to the timelines in Fig. 6). As soon as the high-temperature droplet is deposited onto the relatively cooler substrate, it starts to solidify in the interface region and tensile stresses develop in the droplet, which are a result of the substrate constraining the thermal contraction due to cooling. The substrate, however, experiences an initial phase of heating due to the thermal exchange with the high-temperature droplet, until it reaches a maximum temperature and then cools down to the temperature at its bottom face (500 °C). These heating and cooling cycles occur alternatively in different zones of the substrate. Initially, the top portion of the substrate is heated up to the maximum temperature; this hot region is constrained from a free expansion by the relatively colder portion of the substrate at the bottom, which leads to compressive stresses in this area. Subsequently, the substrate, along with the droplet, cool down to the pre-set temperature. In this phase, the tensile stresses are developed in the top portion of the substrate while the bottom portion is under compression. The cool-down to ambient temperature is not discussed in this study since the droplet and substrate temperatures are already uniform at this stage, thus the further induced residual stresses are not critical. It should be noted that due to the assumed condition of perfect bonding, strain values are equal at the interface,

while they are not necessarily continuous because of the temperature gradient at the interface.

The cross-sectional views of droplet’s deformation (μm) in the Y direction at various times is depicted in Fig. 9 a–c. For better visualisation, the distortion is exaggerated by a factor of 20. As the droplet cools down bottom-up, it undergoes uneven thermal contractions. At only 7 μs from droplet deposition (Fig. 9 a), the solidified material close to the interface contracts, particularly at the periphery of the droplet. Concurrently, the substrate interface, which is bonded to the droplet, experiences an expansion as a result of the droplet’s heat dissipation into the substrate. As cooling continues to the top layers of the droplet, the contraction zones expand. It can be seen in Fig. 9 c that the droplet shrinks in the Z and radial directions where the maximum deformation in Y-direction is 0.63 μm at the steady-state.

Fig. 10 schematically describes the edge delamination process, which is likely to occur during the early stages of solidification, where only a thin layer of the droplet in the vicinity of the interface has solidified. The bending moments created due to uneven contraction and expansion in these regions act as a driving force to lift the droplet at its edges. This happens only if the bending forces are greater than the adhesion forces. As the heat transfer proceeds, these interfacial cracks propagate from the droplet’s edges toward the centre.

To evaluate the likelihood of delamination, the maximum principal stress to temperature-dependent yield strength ratio is used as a criterion. If this ratio is greater than one, the magnitude of the principal stress exceeds the yield strength of the metal, and it is assumed that delamination is likely to occur. This ratio at the Y and Z lines indicated in Fig. 8 are shown in Fig. 11 a–b. It is seen that the failure limit at the interface of droplet and substrate is attained only 27 μs after the droplet deposition. This explains the experimental observation in Fig. 7.

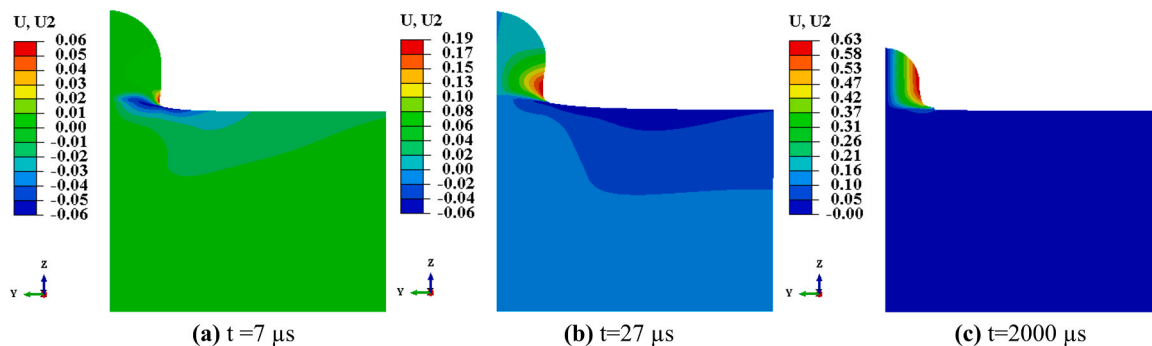


Fig. 9. Cu droplet’s deformation in μm in Y direction exaggerated 20 times at a) 7 μs, b) 27 μs, c) 2000 μs after deposition onto a Cu substrate.

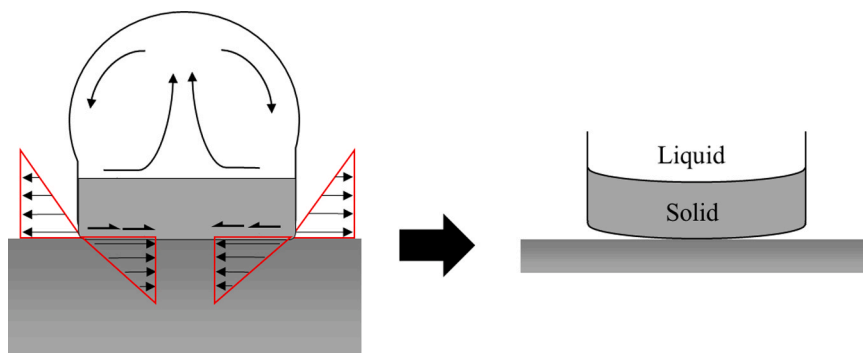


Fig. 10. Schematic representation of the residual stresses (tensile stresses in the droplet and compressive stresses in the substrate) during the early stage of solidification yielding to edge curling. The dashed arrows in the top portion of the droplet indicate the fluid oscillation.

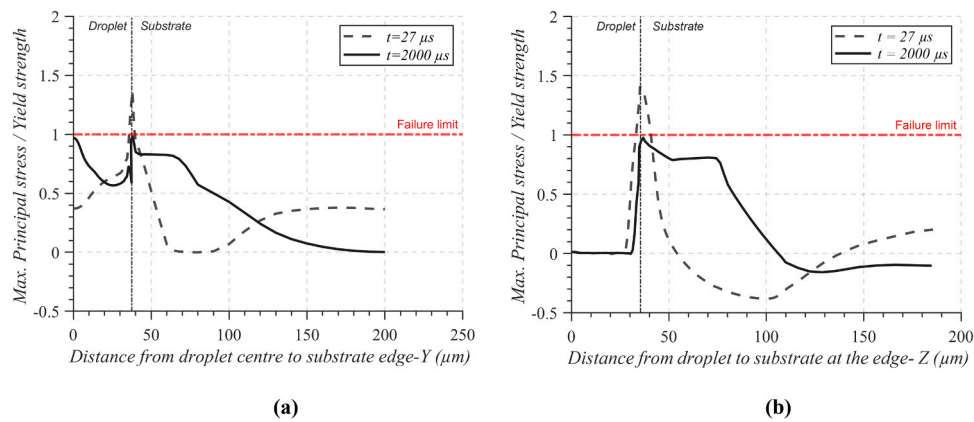


Fig. 11. The maximum principal stress to temperature-dependent yield strength ratio in a) the radial path at the interface of Cu droplet and substrate (Y line shown in Fig. 9), b) droplet and substrate thickness at the edge (Z line is shown in Fig. 9).

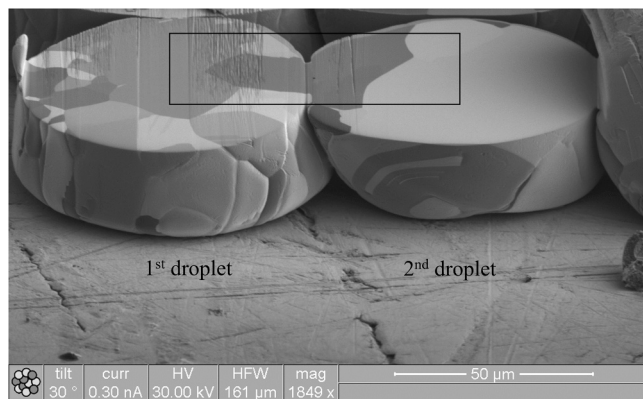


Fig. 12. FIB-SEM cross-section of two successively deposited Cu droplets onto a Cu substrate, demonstrating the lack of remelting at the interface between droplets, and various grain structures for the first and the second droplet. (For interpretation of the references to colour in this figure legend, the reader is referred to the web version of this article.)

3.4. Inter-droplet bonding

The top section of two droplets deposited successively with a frequency of 500 Hz and a centre-to-centre distance of 72 μm, was removed and imaged to investigate inter-droplet bonding. As observed in Fig. 12, the microstructure of the second droplet (*droplet*₂) is quite different to the first droplet (*droplet*₁). The vertical columnar grains observed in *droplet*₁, were replaced by larger grains directed toward the interface in *droplet*₁. Moreover, it seems the neighbouring droplets shared grains at their interface, even though the borders of the droplets were visible at the interface between them.

To clarify this observation, an EBSD analysis was conducted in the

zone indicated with the black square in Fig. 12. The inverse pole figure map (IPF) in the transversal direction (X) of the cross-sectioned sample is shown in Fig. 13. The IPF is a colour-coded representation of the crystallographic orientation of each scanned pixel in respect to a particular spatial coordinate. Here, the X direction corresponds to the heat flux direction at the inter-droplet interface zone. It is confirmed that *droplet*₂ does not melt *droplet*₁ at their interface to form common grains. Moreover, the crystal orientations of interfacial grains are dissimilar, which indicates the absence of epitaxial growth, hence inter-diffusion has not actually happened at the interface as previously thought. Despite the random grain orientation at the interface of the droplet and substrate, low-angle grain boundaries at the interface between droplets were observed.

Cross-sectional views of the temperature profile within the droplets and the substrate during cooling of the second droplet are demonstrated in Fig. 14 a-c. *Droplet*₂ loses heat through contact with the substrate and the preceding droplet, which have already cooled down to the substrate's pre-set temperature. *Droplet*₂ solidifies in a layer-by-layer fashion, bottom-up and side-to-side. During cooling, *droplet*₂ reheats the substrate, *droplet*₁, and also the substrate in contact with *droplet*₁. *Droplet*₁ is entirely reheated to some extent, however, the interface with *droplet*₂ is where the highest temperature is attained (Fig. 14 d). It is also seen that the top section of the droplets' interface is heated to the highest value of 833 °C, while closer to the substrate interface, the maximum temperature is 825 °C. Indeed, in the top segment, the energy transformed into *droplet*₁ through the interface is uniquely invested in heating this zone, whereas in the bottom section, this energy is split into heating the substrate and *droplet*₁.

During cooling of the second droplet, the substrate temperature reaches the highest value of 763 °C at the interface with *droplet*₂ while this value was 766 °C at the interface with *droplet*₁ during cooling of the first droplet. This slight difference is due to the inter-droplet heat exchange during the cooling of *droplet*₂. Also, as depicted in Fig. 15, the

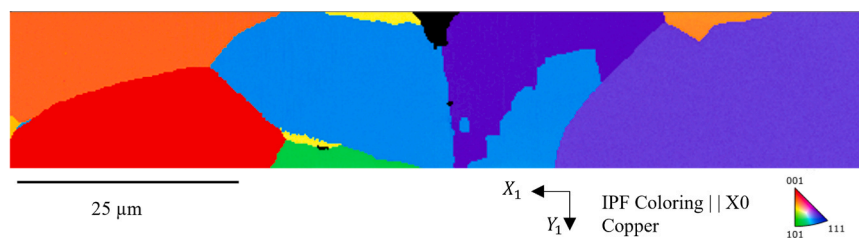


Fig. 13. EBSD IPF-X map of two successively deposited Cu droplets in the region highlighted in Fig. 12, indicating the absence of epitaxy at the interface between droplets.

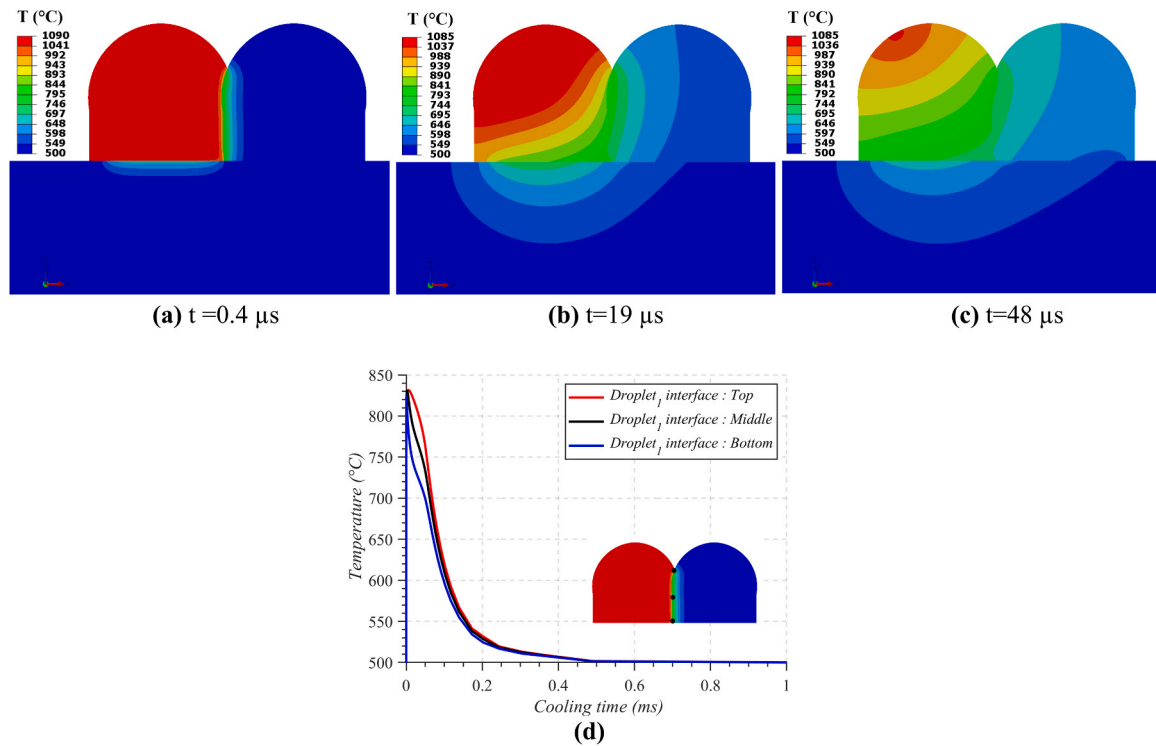


Fig. 14. Cross-section profile views of temperature whilst second Cu droplet solidification onto a Cu substrate, taken at a real-time of a) $t = 0.4 \mu s$, b) $t = 19 \mu s$, c) $t = 48 \mu s$, d) temperature evolution of various nodes at droplet₁'s interface with droplet₂ in the bottom, middle, and top sections.

cooling rates of the first and second droplets at the central node are slightly different. The faster cooling of droplet₂ is justified by its increased contact with colder surfaces.

The thermal resistance at the interface between the droplets is lower than that at the substrate interface, due to the surface roughness dissimilarity. The surface of solidified droplets is smoother compared to the surface of polished substrates. Although the droplet's surface is not perfectly flat due to the solidification ripples, it does not induce an important contact resistance at droplets' interface since the molten droplet can spread in between the ridges and fill the gaps. Contrarily, the microscale and nanoscale asperities present on the substrate surface, act as a thermal exchange barrier because they cannot be filled with liquid metal due to its high surface tension. In addition, the bottom segment of

droplets, where two droplets come into contact, is ripple-free. Consequently, the interface between droplets reaches a higher temperature of 833 °C, compared to 763 °C at the substrate interface. This is possibly the reason for the formation of elongated grains with low-angle boundaries at the inter-droplet interface compared to the heterogenous grains at the droplet-substrate interface.

4. Conclusions

Various features of single and multiple copper droplets deposited onto a copper substrate using the DoD MetalJet system were experimentally investigated. The experimental observations that could not be thoroughly explained were assessed using a sequentially coupled FE thermo-mechanical model. This provided complementary insights into some aspects of the process, which were not understood to date. Specific conclusions were drawn from the research:

- Individual droplets were loosely attached to the substrate, indicating insufficient energy at the interface to melt the substrate and promote metallurgical bonding. Numerical results revealed the maximum attained temperature at the interface of the droplet and substrate fell short of the melting point of Cu.
- Even though a strong droplet-to-droplet bonding through remelting or epitaxial growth at the droplets' interface was not achieved, the numerical results showed the higher interfacial temperatures in this zone provide a better level of bonding compared to the droplet-substrate bonding. This was also observed in the FIB-SEM images, where elongated grains with low-angle boundaries were observed at the inter-droplet interface.
- Residual stresses were developed due to steep temperature gradients during the deposition and cooling processes. It is likely that uneven contraction and expansion at the vicinity of the interface lift the droplet at its edges. Due to the high magnitude of thermal stresses at the droplet-substrate interface, which exceeds the elastic limits of the

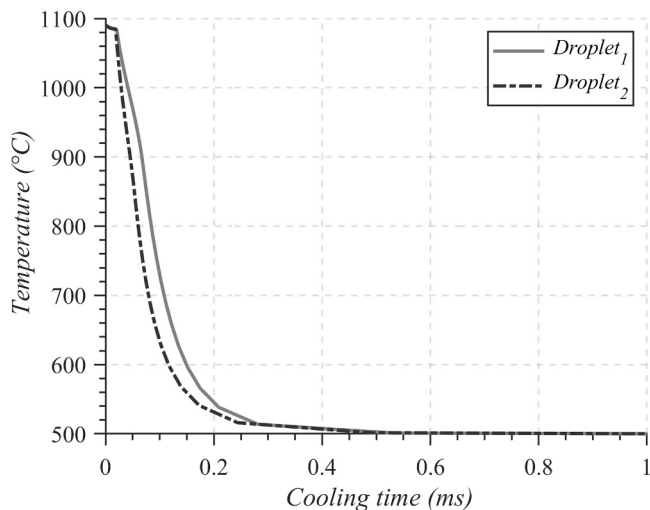


Fig. 15. Temperature evolution of nodes at the centre of Cu droplets during the deposition of droplet₁ and droplet₂ onto a Cu substrate.

material, residual-stress-induced delamination seems to occur. This is also confirmed by the experimental observations.

CRedit authorship contribution statement

Negar Gilani: Conceptualization, Methodology, Software, Investigation, Formal analysis, Writing – original draft. **Nesma. T. Aboulkhair:** Supervision, Investigation, Writing – review & editing, Funding acquisition. **Marco Simonelli:** Supervision, Writing – review & editing. **Ian A. Ashcroft:** Supervision, Writing – review & editing, Funding acquisition. **Mark East:** Resources. **Richard J.M. Hague:** Supervision, Writing – review & editing, Project administration, Funding acquisition.

Declaration of Competing Interest

Authors declare no competing interests.

Appendix A

A1. Thermal model validation

An FIB secondary image of a cross-sectioned Sn droplet deposited at 655 °C onto a Sn substrate at 50 °C is shown in Fig. A1 a. The droplet-substrate interface, indicated by the black arrows, is partially visible, implying that the substrate did not melt during droplet deposition in this zone. In this case, ~14 μm of the contact line is melted and ~25 μm is not melted. As per Fig. A1 b, the length of the melted interface has increased for the Sn droplet deposited at 755 °C onto a Sn substrate at 50 °C. In this case, the droplet melted the contact surface up to a radius of ~26 μm from the centre and only ~9 μm remained un-melted. As the deposition temperature was increased to 955 °C (Fig. A1 c), the entire Sn substrate interface was melted.

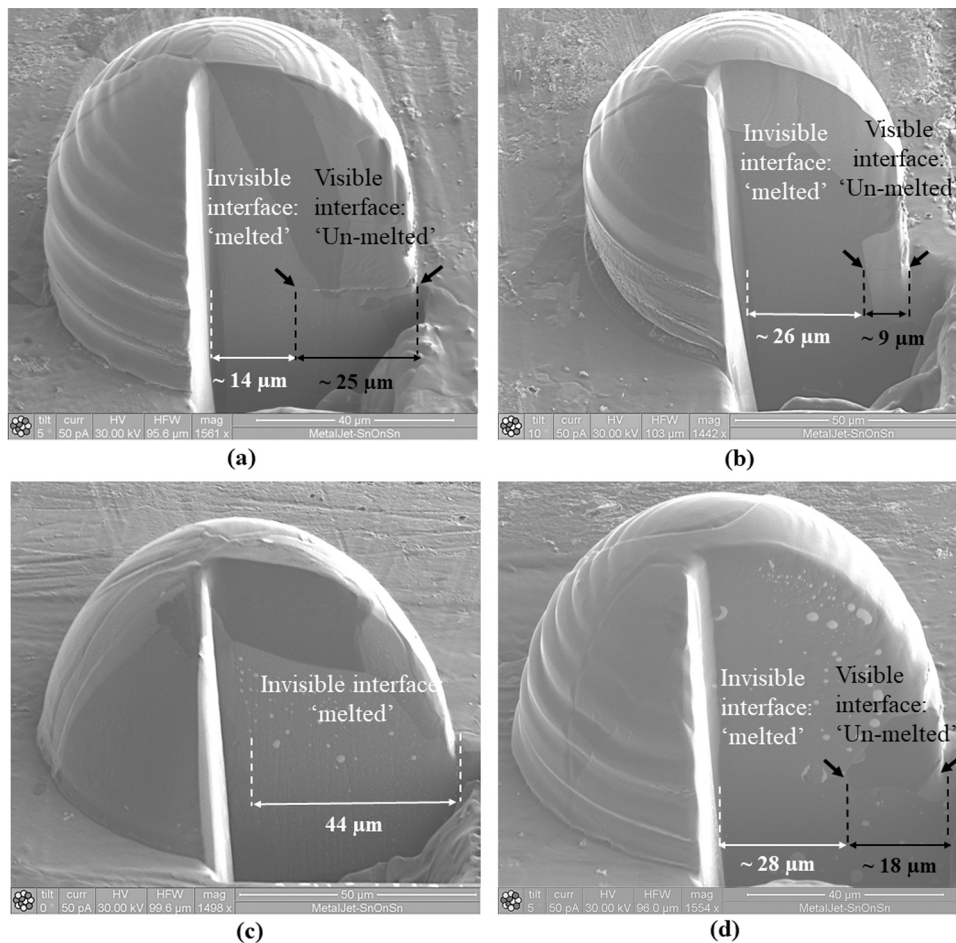


Fig. A1. FIB-SEM cross-section of individual Sn droplets deposited on a Sn substrate **a)** $T_{drop} = 655^{\circ}\text{C}$ and $T_{substrate} = 50^{\circ}\text{C}$ indicating partial remelting of the substrate interface, and **b)** $T_{drop} = 755^{\circ}\text{C}$ and $T_{substrate} = 50^{\circ}\text{C}$ indicating partial remelting of the substrate interface, **c)** $T_{drop} = 955^{\circ}\text{C}$ and $T_{substrate} = 50^{\circ}\text{C}$ indicating complete remelting of the substrate interface, and **d)** $T_{drop} = 655^{\circ}\text{C}$ and $T_{substrate} = 100^{\circ}\text{C}$ indicating partial remelting of the substrate interface.

Alternatively, the interface of a Sn droplet at 655 °C deposited onto a Sn substrate at 100 °C was investigated. In Fig. A1 d, the interface is partially visible, implying partial substrate melting. Here, the molten droplet melted the contact surface up to a radius of ~28 μm from the droplet centre, but an annulus of ~18 μm remained un-melted. In the un-melted zone, the grains within the droplet nucleated at the interface with the substrate. Whereas in the melted section, common grains formed from the inner zone of the substrate.

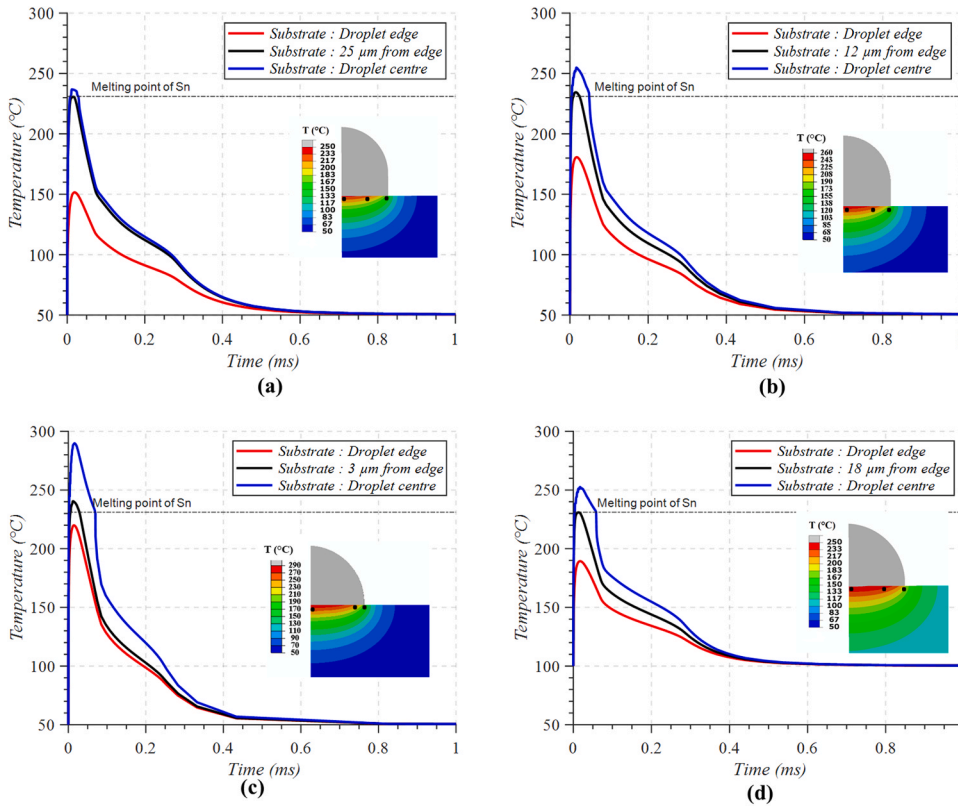


Fig. A2. Sn substrate temperature evolution at the interface of a Sn droplet when: **a)** $T_{drop} = 655^{\circ}C$ and $T_{substrate} = 50^{\circ}C$ for nodes below the droplet centre, 25 μm from the droplet edge, and the droplet edge, **b)** $T_{drop} = 755^{\circ}C$ and $T_{substrate} = 50^{\circ}C$ for nodes below the droplet centre, 12 μm from the droplet edge, and the droplet edge, **c)** $T_{drop} = 955^{\circ}C$ and $T_{substrate} = 50^{\circ}C$ for nodes below the droplet centre, 3 μm from the droplet edge, and the droplet edge, and **d)** $T_{drop} = 655^{\circ}C$ and $T_{substrate} = 100^{\circ}C$ for nodes below the droplet centre, 18 μm from the droplet edge, and the droplet edge.

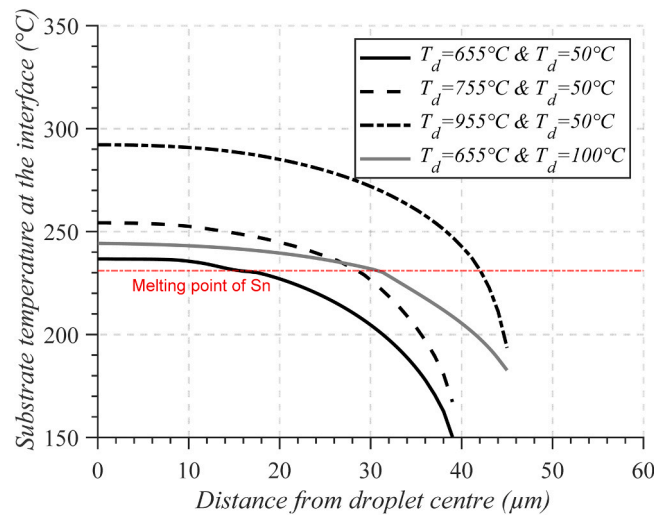


Fig. A3. Sn substrates temperature at the interface with Sn droplets in the radial distance from the droplet centre for various scenarios in Fig. A2.

The four scenarios shown in Fig. A1 were simulated using the thermal FE model. In Fig. A2 a-d, three locations on the surface of the substrate are chosen, two of which correspond to the warmest and coldest nodes. These nodes are below the centre and the edge of the droplet, respectively. The third node is where the substrate temperature reaches the melting point of Sn. From this location toward the droplet's edge, the substrate temperature remains below the melting point of Sn. As illustrated in Fig. A2 a, for $T_{\text{droplet}} = 655^{\circ}\text{C}$ and $T_{\text{substrate}} = 50^{\circ}\text{C}$, the interface temperature remains below the melting point of Sn up to a periphery of 25 μm from the droplet's edge during the droplet cooling and solidification. The un-melted interface is 12 μm and 3 μm from the droplet's edge as the droplets temperature increase to 755 $^{\circ}\text{C}$ (Fig. A2 b) and 955 $^{\circ}\text{C}$ (Fig. A2 c), respectively, with the substrate at 50 $^{\circ}\text{C}$. Fig. A2 d demonstrates the interface temperature evolution when $T_{\text{droplet}} = 655^{\circ}\text{C}$ $T_{\text{substrate}} = 100^{\circ}\text{C}$. It is seen that the interface below the droplet centre exceeds the melting temperature of Sn. The same behaviour is observed up to a periphery of 28 μm from the centre.

The interface temperature in the radial distance from the droplet centre is demonstrated in Fig. A3 for the cases described in Figs. A1 and A2. In these graphs, the melted regions are above the melting point of Sn. It is therefore demonstrated that the numerical results match the experimental observations, providing some confidence going forwards in the modelling approach used.

The thermophysical properties used for the model validation are presented in Table A1.

Table A1
Temperature-dependent properties of pure Sn.

| Temperature ($^{\circ}\text{C}$) | 27 | 232 | 327 | 1127 |
|--|------|-------|-------|-------|
| Density (kg/m^3) | 7300 | 6900 | 6850 | 6300 |
| Heat capacity ($\text{J}/\text{kg } ^{\circ}\text{C}$) | 207 | 210.1 | 211.9 | 233.5 |
| Thermal conductivity ($\text{W}/\text{m } ^{\circ}\text{C}$) | 66.6 | 56 | 95.7 | 163.2 |
| Surface tension (N/m) | – | 0.546 | 0.540 | 0.480 |

References

- [1] K.S. Schmaltz, L.J. Zarzalejo, C.H. Amon, Molten droplet solidification and substrate remelting in microcasting Part II: parametric study and effect of dissimilar materials, *Heat Mass Transf.* 35 (1999) 17–23.
- [2] C.-J. Li, G.-J. Yang, C.-X. Li, Development of particle interface bonding in thermal spray coatings: a review, *J. Therm. Spray. Technol.* vol. 22 (2013) 192–206.
- [3] J.W. Priest, C. Smith, P. Dubois, Liquid metal jetting for printing metal parts, in: *Solid Freeform Fabrication Proceedings*, University of Texas at Austin, TX, (1997), pp. 1–10.
- [4] A. Amirzadeh, M. Raessi, S. Chandra, Producing molten metal droplets smaller than the nozzle diameter using a pneumatic drop-on-demand generator, *Exp. Therm. Fluid Sci.* 47 (2013) 26–33 (May).
- [5] S. Zhong, L. Qi, J. Luo, H. Zuo, X. Hou, H. Li, Effect of process parameters on copper droplet ejecting by pneumatic drop-on-demand technology, *J. Mater. Process. Technol.* 214 (12) (2014) 3089–3097 (Dec.).
- [6] S.I. Moqadam, L. Madler, N. Ellendt, A high temperature drop-on-demand droplet generator for metallic melts, *Micromachines* 10 (2019).
- [7] J. Luo, W. Wang, W. Xiong, H. Shen, L. Qi, Formation of uniform metal traces using alternate droplet printing, *Int. J. Mach. Tools Manuf.* 122 (2017) 47–54 (Nov.).
- [8] K. Yamaguchi, K. Sakai, T. Yamanaka, T. Hirayama, Generation of three-dimensional micro structure using metal jet, *Precis. Eng.* 24 (1) (1999) 2–8 (Jan.).
- [9] I.H. Karamelas, et al., Drop-on-demand 3D metal printing, *Tech. Connect Briefs* 4 (2017) 153–155.
- [10] Z. Luo, X. Wang, L. Wang, D. Sun, Z. Li, Drop-on-demand electromagnetic printing of metallic droplets, *Mater. Lett.* 188 (2017) 184–187 (Feb.).
- [11] V. Sukhotskiy, P. Vishnoi, I.H. Karamelas, S. Vader, Z. Vader, E.P. Furlani, Magnetohydrodynamic drop-on-demand liquid metal additive manufacturing: system overview and modelling, in: *Proceedings of the 5th International Conference of Fluid Flow, Heat and Mass Transfer (FFHMT'18)*, (2018).
- [12] M. Simonelli, et al., Towards digital metal additive manufacturing via high-temperature drop-on-demand jetting, *Addit. Manuf.* 30 (2019) (Dec.).
- [13] M.V. Rasa, R. Berkhout, W.P. J. Classens, C.M. Van, H. Genuchten, E.V. Kuznetsov, Device for ejecting droplets of a fluid having high temperature, US 2011/0233239 A1, (2013).
- [14] G. Trapaga, E.F. Matthys, J.J. Valencia, J. Szekely, Fluid flow, heat transfer, and solidification of molten metal droplets impinging on substrates: comparison of numerical and experimental results, *Metall. Trans. B* 23B (1992).
- [15] A. Kumar, S. Ghosh, B.K. Dhindaw, Simulation of cooling of liquid Al-33 wt% Cu droplet impinging on a metallic substrate and its experimental validation, *Acta Mater.* 58 (2009) 122–133.
- [16] M. Pasandideh-Fard, S. Chandra, J. Mostaghimi, A three-dimensional model of droplet impact and solidification, *Int. J. Heat Mass Transf.* 45 (11) (2002) 2229–2242 (May).
- [17] H. Li, P. Wang, L. Qi, H. Zuo, S. Zhong, X. Hou, 3D numerical simulation of successive deposition of uniform molten Al droplets on a moving substrate and experimental validation, *Comput. Mater. Sci.* 65 (2012) 291–301.
- [18] Y.Z. Zheng, Q. Li, Z.H. Zheng, J.F. Zhu, P.L. Cao, Modeling the impact, flattening and solidification of a molten droplet on a solid substrate during plasma spraying, *Appl. Surf. Sci.* 317 (2014) 526–533 (Oct.).
- [19] B. Kang, J. Waldvogel, D. Poulikakos, Remelting phenomena in the process of splat solidification, *J. Mater. Sci.* 30 (19) (1995) 4912–4925 (Oct.).
- [20] C.H. Amon, K. Schmaltz, R. Merz, F.B. Prinz, Numerical and experimental investigation of interface bonding via substrate remelting of an impinging molten metal droplet, *J. Heat Transf.* (1996).
- [21] L.J. Zarzalejo, K.S. Schmaltz, C.H. Amon, Molten droplet solidification and substrate remelting in microcasting Part I: numerical modeling and experimental verification, *Heat Mass Transf.* 34 (1998) 477–485.
- [22] Q. Xu, V. Gupta, E. Lavernia, Thermal behavior during droplet-based deposition, *Acta Mater.* 48 (4) (2000) 835–849 (Feb.).
- [23] R.K. Chin, J.L. Beuth, C.H. Amon, Thermomechanical modeling of molten metal droplet solidification applied to layered manufacturing, *Mech. Mater.* 24 (4) (1996) 257–271 (Dec.).
- [24] R.K. Chin, J.L. Beuth, C.H. Amon, Thermomechanical modeling of successive material deposition in layered manufacturing, in: *International Solid Freeform Fabrication Symposium*, (1996).
- [25] R.K. Chin, J.L. Beuth, C.H. Amon, Successive deposition of metals in solid freeform fabrication processes, part 1: thermomechanical models of layers and droplet columns, *J. Manuf. Sci. Eng.* 123 (2001).
- [26] M.P. Mughal, H. Fawad, R. Mufti, Finite element prediction of thermal stresses and deformations in layered manufacturing of metallic parts, *Acta Mech.* 183 (2006) 61–79.
- [27] W. Wang, R.A. Lambert, R.H. Rangel, Parametric study of multi-splat solidification/remelting including contact resistance effects, *Int. J. Heat Mass Transf.* 51 (19–20) (2008) 4811–4819 (Sep.).
- [28] S.D. Aziz, S. Chandra, Impact, recoil and splashing of molten metal droplets, *Int. J. Heat Mass Transf.* 43 (16) (2000) 2841–2857 (Aug.).
- [29] M. Xue, Y. Heichal, C. Sanjeev, J. Mostaghimi, Modeling the impact of a molten metal droplet on a solid surface using variable interfacial thermal contact resistance, *J. Mater. Sci.* 42 (2007) 9–18.
- [30] Li M., S.J. Zinkle, Physical and mechanical properties of copper and copper alloys, in: *Comprehensive Nuclear Materials*, vol. 4, (2012).
- [31] H.P. Li, H.J. Li, L.H. Qi, J. Luo, H.S. Zuo, Simulation on deposition and solidification processes of 7075 Al alloy droplets in 3D printing technology, *Trans. Nonferrous Met. Soc. China* 24 (6) (2014) 1836–1843 (English Ed.).
- [32] S. Schiaffino, A.A. Sonin, Molten droplet deposition and solidification at low Weber numbers, *Phys. Fluids* 9 (1997) 3172.
- [33] J.W. Elmer, J. Klingmann, K. Van Bibber, Diffusion bonding and brazing of high purity copper for linear collider accelerator structures, *Phys. Rev. Spec. Top. Accel. Beams* 4 (5) (2001), 053502 (May).